A&A 413, 733–743 (2004)
DOI: 10.1051/0004-6361:20031570

Astronomy & Astrophysics

Radiative transfer in cylindrical threads with incident radiation

P. Gouttebroze⋆

Institut d'Astrophysique Spatiale, Univ. Paris XI/CNRS, Bât. 121, 91405 Orsay Cedex, France

Received 6 May 2003 / Accepted 23 September 2003

Abstract. Methods for the solution of non-LTE radiative transfer equations in a cylinder, with external incident radiation, have been developed in the framework of accelerated Λ-iteration methods. This paper is restricted to the so-called one-dimension problem. The first method under investigation treats a two-level atom in the Eddington approximation: the comparison of results with a semi-analytical method (restricted to homogeneous cylinders) is used to study the effects of radius discretization. The second method removes the Eddington approximation and uses detailed (multiray) angular integration of intensities. Finally, the method is extended to a multilevel atom with a treatment of radiative transfer in both lines and continua. It is applied to a model hydrogen atom with 20 levels and one continuum, with correction of the electron density. Convergence properties and results are discussed.

Key words. methods: numerical – radiative transfer – line: profiles – line: formation

1. Introduction

In the solar external atmosphere, the plasma is structured by the magnetic field, which produces thread-like objects (coronal loops). Solar prominences, as seen on Hα spectroheliograms, seem also to be filled with such structures. The usual way to treat radiative transfer in cylindrical structures consists of replacing the cylinder by a plane-parallel slab whose thickness is equal to its diameter. This approximation gives the correct order of magnitude for the source functions and emergent intensities, but errors of about 30% are common (see, e.g., Gouttebroze et al. 1986). So, it is justified to develop specific radiative transfer methods for cylindrical objects, in order to remove this uncertainty.

The radiative transfer problem treated here is the so-called 1-dimension problem, which means that the radiation field is invariant by rotation around the axis of the cylinder and by translation along this axis. This is the case for a vertical thread in the solar atmosphere, which receives incident radiation independent of the azimuth (invariance by rotation) and whose length is small compared to the radius of the Sun, so that the variation of the dilution factor with altitude may be neglected (invariance by translation). This problem has been treated in particular by Heaslet & Warming (1966), who derived basic equations and provided analytic solutions for some special cases. Leung (1975) developed a method based on variable Eddington factors, using a Feautrier-type finite difference scheme, then suppressing the limitations of the Eddington approximation, and allowing a radial variation of basic parameters (temperature, pressure, electron density, etc.). Heasley (1976) used almost the same method, but extended it to multilevel problems, treating a five-level Ca II ion. In a previous paper (Gouttebroze 1990, hereafter G90), we proposed a semi-analytical method, similar to the method of Wick (1943) or Chandrasekhar (1950) for plane-parallel slabs, but using Bessel functions instead of exponentials. This method allows partial frequency redistribution, but is restricted to the Eddington approximation and homogeneous models.

During the past 15 or 20 years, methods based on the principle of accelerated Λ-iteration (ALI) have gradually replaced previous methods using matrix inversions, such as the Feautrier method or integral equations methods. These ALI methods have been recently reviewed by Hubeny (2003) and Paletou (2001, in french). Concerning cylinders, a method has been recently proposed by van Noort et al. (2002). It allows different geometries (planar, spherical and cylindrical) and two or three dimensions, but is restricted to a two-level atom for the moment. The method presented here is restricted to one dimension, but includes radiative transfer in both lines and continua, solution of statistical equilibrium equations, and self-consistent determination of the electron density (in the case of the hydrogen atom). It aims at the modelling of solar coronal loops and prominence threads.

2. The cylindrical 1-dimension problem

2.1. Radiative transfer equation

The time-independent radiative transfer equation may be written quite generally:

$$\boldsymbol{n}.\boldsymbol{\nabla} I_\nu = -\kappa_\nu (I_\nu - S_\nu) \tag{1}$$

where ν is the frequency, $\boldsymbol{n}$ the direction of the ray, I_ν the specific intensity, κ_ν the absorption coefficient, and S_ν the source function.

⋆ e-mail: goutte@ias.u-psud.fr

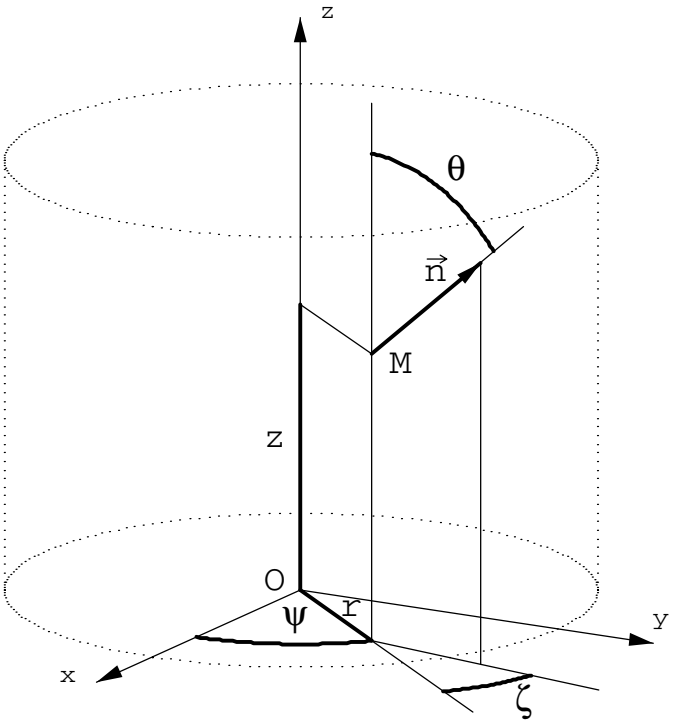

Fig. 1. System of cylindrical coordinates.

In cylindrical coordinates, the running point $\boldsymbol{M}$ is represented by three quantities: r, ψ and z, and the direction of the ray by two angles: the colatitude θ and ζ, which is the angle between the local meridian plane and the vertical plane containing the ray (Fig. 1). The expansion of Eq. (1) in terms of these variables gives:

$$\sin\theta\cos\zeta\frac{\partial I_\nu}{\partial r}+\frac{\sin\theta\sin\zeta}{r}\frac{\partial I_\nu}{\partial\psi}+\cos\theta\frac{\partial I_\nu}{\partial z} -\frac{\sin\theta\sin\zeta}{r}\frac{\partial I_\nu}{\partial\zeta}=-\kappa_\nu\left(I_\nu-S_\nu\right). \quad (2)$$

In this paper, we study the "1-dimension" problem: if I_ν is invariant by translation along the axis of the cylinder and by rotation around it, derivatives in z and ψ vanish and the equation reduces to:

$$\sin\theta\left(\cos\zeta\frac{\partial I_\nu}{\partial r}-\frac{\sin\zeta}{r}\frac{\partial I_\nu}{\partial\zeta}\right)=-\kappa_\nu\left(I_\nu-S_\nu\right). \quad (3)$$

2.2. Source function

We consider the formation of the line of a two-level atom, in complete redistribution, and without continuous absorption. So, the source function may be written:

$$S_\nu=S=\epsilon B+(1-\epsilon)\bar{J} \quad (4)$$

with:

$$\bar{J}=\int_0^\infty J_\nu\,\phi_\nu\,\mathrm{d}\nu \quad (5)$$

where ϵ and B are given parameters, ϕ_ν is the absorption profile, and J_ν the direction averaged intensity:

$$J_\nu(r)=\oint I_\nu\frac{\mathrm{d}\Omega}{4\pi}=\frac{1}{4\pi}\int_0^{2\pi}\mathrm{d}\zeta\int_0^\pi I_\nu(r,\theta,\zeta)\sin\theta\,\mathrm{d}\theta. \quad (6)$$

The parameters ϵ, B and ϕ_ν vary with r, except in the *homogeneous* case.

2.3. Boundary conditions

The cylinder is irradiated by an isotropic (or simply azimuth-independent) incident radiation, which provides the external boundary condition:

$$I_\nu(R,\theta,\pi+\zeta)=J_\nu^{\mathrm{inc}},\quad\left(0<\theta<\pi,-\frac{\pi}{2}<\zeta<\frac{\pi}{2}\right) \quad (7)$$

(R being the radius of the cylinder).
Along the axis, I_ν becomes independent of ζ, which provides the internal boundary condition:

$$I_\nu(r=0,\theta,\zeta)=I_\nu(r=0,\theta,\zeta=0). \quad (8)$$

3. Methods based on the Eddington approximation

3.1. Moment equations

Equations for the moments of intensity may be obtained from Eq. (3) by angular integration. If we define the operator:

$$M^{(n)}=\frac{1}{4\pi}\int_0^{2\pi}\cos^n\zeta\mathrm{d}\zeta\int_0^\pi\sin^{n+1}\theta\,\mathrm{d}\theta\{\}, \quad (9)$$

the three first moments of intensity are: $J_\nu=M^{(0)}\{I_\nu\}$, $H_\nu=M^{(1)}\{I_\nu\}$ and $K_\nu=M^{(2)}\{I_\nu\}$. In the cylindrical case, it is necessary to define the following quantity (cf. Leung 1976):

$$Q_\nu=\frac{1}{4\pi}\int_0^{2\pi}\mathrm{d}\zeta\int_0^\pi I_\nu\,\sin^3\theta\,\mathrm{d}\theta. \quad (10)$$

Applications of operators $M^{(0)}$ and $M^{(1)}$ to Eq. (3) yield respectively:

$$\frac{1}{r}\frac{\partial}{\partial r}\left(rH_\nu\right)=-\kappa_\nu\left(J_\nu-S_\nu\right) \quad (11)$$

and

$$\frac{\partial K_\nu}{\partial r}+\frac{2K_\nu-Q_\nu}{r}=-\kappa_\nu H_\nu. \quad (12)$$

3.2. Semi-analytical (SA) method

The Eddington approximation consists of assuming that the intensity is constant both in the inward and the outward half-space, i.e., for $-\pi/2\le\zeta\le\pi/2$:

$$\begin{aligned} I_\nu(r,\theta,\zeta) &= I_\nu^+(r),\\ I_\nu(r,\theta,\pi+\zeta) &= I_\nu^-(r), \end{aligned} \quad (13)$$

which gives the following relations between the intensity and its moments:

$$\begin{aligned} I_\nu^+ + I_\nu^- &= 2J_\nu = 6K_\nu = 3Q_\nu,\\ I_\nu^+ - I_\nu^- &= 4H_\nu. \end{aligned} \quad (14)$$

In this way, the radiative transfer equation for I_ν reduces to an equation for the angle-averaged intensity J_ν:

$$\frac{1}{r\kappa_\nu}\frac{\partial}{\partial r}\left(\frac{r}{\kappa_\nu}\frac{\partial J_\nu}{\partial r}\right)=3\left(J_\nu-S_\nu\right). \quad (15)$$

The corresponding boundary conditions are:

$$\left[\frac{\partial J_\nu}{\partial r}\right]_{r=0} = 0 \tag{16}$$

and:

$$J_\nu(R) + \frac{2}{3\kappa_\nu}\left[\frac{\partial J_\nu}{\partial r}\right]_{r=R} = J_\nu^{\rm inc}. \tag{17}$$

If κ_ν does not depend on r (homogeneous models), Eq. (15) reduces to the formula given in G90:

$$\frac{\partial^2 J_\nu}{\partial r^2} + \frac{1}{r}\frac{\partial J_\nu}{\partial r} = 3\,\kappa_\nu^2\,(J_\nu - S_\nu)\,. \tag{18}$$

In G90, we described a semi-analytical (SA) method for homogeneous cylinders, in the Eddington approximation. In this method, the mean intensity is expanded as a sum of Bessel functions of the radius $I_0(kr)$, so that the solution is obtained without the use of any spatial grid.

3.3. Radius discretization

The methods described below use the ALI principle and are based on finite-difference schemes. The precision of these schemes depends on the choice of the spatial grid, so that some attention must be paid to the definition of this grid. In the interior of the cylinder, a linear mesh is sufficient but, close to the surface, a logarithmic mesh is necessary, as in the case of a plane-parallel slab. So, we use a combination of linear and logarithmic meshes: the linear section covers the major part of the total radius R, from $r = 0$ to $r = 0.9R$. In the remaining external part of the cylinder, the steps decrease exponentially towards the exterior. To study the influence of mesh spacing on the results, we use an automatic definition of this mesh based on an integer parameter α, which represents the number of points per decade in the external region. The thickness of the outermost layer $\Delta r_{\rm min}$ is chosen in such a way that $(R/\Delta r_{\rm min}) = 10^\beta$, where β is an integer, so that $(\beta - 1)$ is the number of decades in the logarithmic region. We complete the definition of the mesh in order to have approximately the same number of points (i.e. $(\beta - 1)\alpha$) in the linear part as in the logarithmic one, and set $r_1 = 0$. Finally, the generating algorithm is:

$$\begin{aligned}
&\gamma = (\beta-1)\alpha,\\
&\delta = 0.1^{1/\alpha},\\
&r_j = 0.9R\frac{j-1}{\gamma-1}, \qquad (j = 1,\ldots,\gamma),\\
&r_j = R(1-\delta) + r_{j-1}\delta, \qquad (j = \gamma+1,\ldots,2\gamma),\\
&r_{2\gamma+1} = R.
\end{aligned} \tag{19}$$

3.4. Eddington approximation finite-difference (EAFD) method

We consider Eq. (15) for a given frequency ν and discretise it with respect to r (the index "ν" is omitted for convenience). The derivatives in Eq. (15) are replaced by difference ratios. If N is the total number of points of the r-grid ($N = 2\gamma + 1$ in the preceding formulae), we set, for $2 \le j \le N-1$:

$$\left[\frac{\partial}{\partial r}\left(\frac{r}{\kappa}\frac{\partial J}{\partial r}\right)\right]_j \approx \frac{2}{r_{j+1} - r_{j-1}} \times\left(\frac{r_j + r_{j+1}}{\kappa_j + \kappa_{j+1}}\frac{J_{j+1} - J_j}{r_{j+1} - r_j} - \frac{r_{j-1} + r_j}{\kappa_{j-1} + \kappa_j}\frac{J_j - J_{j-1}}{r_j - r_{j-1}}\right). \tag{20}$$

If we substitute this formula into Eq. (15), we obtain the usual tridiagonal system:

$$-A_j J_{j-1} + B_j J_j - C_j J_{j+1} = S_j,\ (j = 2,\ldots,N-1) \tag{21}$$

with:

$$\begin{aligned}
A_j &= \frac{2\left(r_{j-1} + r_j\right)}{3\kappa_j r_j\left(r_{j+1} - r_{j-1}\right)\left(\kappa_{j-1} + \kappa_j\right)\left(r_j - r_{j-1}\right)},\\
C_j &= \frac{2\left(r_j + r_{j+1}\right)}{3\kappa_j r_j\left(r_{j+1} - r_{j-1}\right)\left(\kappa_j + \kappa_{j+1}\right)\left(r_{j+1} - r_j\right)},\\
B_j &= 1 + A_j + C_j.
\end{aligned} \tag{22}$$

In order to complete this tridiagonal system, we discretise the boundary conditions (16) and (17). Near the axis of the cylinder, we approximate $J(r)$ by a second degree polynomial:

$$J(r) = a_0 + a_1 r + a_2 r^2, \tag{23}$$

so that Eq. (16) gives $a_1 = 0$. Since $r_1 = 0$, we have $J_1 = a_0$ and $J(r) = J_1 + a_2 r^2$. Substituting this expression into Eq. (15), and neglecting the variation of κ between r_1 and r_2, we eliminate a_2 and obtain the following relation between J_1 and J_2:

$$B_1 J_1 - C_1 J_2 = S_1 \tag{24}$$

with:

$$C_1 = \frac{4}{3\,\kappa_1^2\,r_2^2} \quad \text{and} \quad B_1 = C_1 + 1. \tag{25}$$

We use a similar approximation between r_{N-1} and r_N ($= R$) and combine Eqs. (15) and (17) to obtain:

$$-A_N J_{N-1} + B_N J_N = S_N + H_N J^{\rm inc} \tag{26}$$

with:

$$\begin{aligned}
A_N &= \frac{2}{3\kappa_N^2 (r_N - r_{N-1})^2},\\
H_N &= \frac{1}{\kappa_N}\left(\frac{1}{r_N - r_{N-1}} + \frac{1}{2r_N}\right),\\
B_N &= 1 + A_N + H_N.
\end{aligned} \tag{27}$$

Finally, we have a complete tridiagonal system for each frequency:

$$-A_j J_{j-1} + B_j J_j - C_j J_{j+1} = S_j + H_j J^{\rm inc} \tag{28}$$

where H_N is the only nonzero element of the vector $\boldsymbol{H}$. To solve numerically the system for all frequencies, we introduce a frequency mesh ($\nu_\gamma, \gamma = 1,\ldots,n$) and a quadrature formula (coefficients c_γ^j) which transforms Eq. (5) into:

$$\bar{J}_j = \sum_{\gamma=1}^{n} c_\gamma^j J_j^\gamma. \tag{29}$$

As in the plane-parallel case, there are several ways to solve the system of Eqs. (4)+(28)+(29): direct method, Λ-iteration and ALI.

Direct method. Following Rybicki (1971), we consider the system (28) as a product of a matrix by a vector $\boldsymbol{T}^\gamma \boldsymbol{J}^\gamma = \boldsymbol{S} + \boldsymbol{H} J_\gamma^{\rm inc}$, and invert the matrices $\boldsymbol{T}^\gamma$ to get $\boldsymbol{U}^\gamma$, so that:

$$J_j^\gamma = \sum_{k=1}^{N} U_{jk}^\gamma \left(S_k + H_k^\gamma J_\gamma^{\rm inc} \right). \tag{30}$$

Combination of this equation with Eqs. (4) and (29) yields:

$$S_j = \epsilon_j B_j + \left(1-\epsilon_j\right) \sum_{k=1}^{N} \Lambda_{jk} S_k + \left(1-\epsilon_j\right) \Gamma_j \tag{31}$$

with:

$$\Lambda_{jk} = \sum_{\gamma=1}^{n} c_\gamma^j U_{jk}^\gamma \tag{32}$$

and:

$$\Gamma_j = \sum_{\gamma=1}^{n} c_\gamma^j U_{jN}^\gamma H_N^\gamma J_\gamma^{\rm inc}. \tag{33}$$

Equation (31) constitutes a linear system:

$$\sum_{k=1}^{N} M_{jk} S_k = \epsilon_j B_j + \left(1-\epsilon_j\right) \Gamma_j \tag{34}$$

with:

$$M_{jk} = \delta_{jk} - \left(1-\epsilon_j\right) \Lambda_{jk} \tag{35}$$

(δ_{jk} is the Kronecker symbol).
The linear system (34) may be solved for S_j by a direct method. This process, including matrix inversions, is not fast enough for our purpose, but may be used as a reference for checking the convergence of other methods.

Λ-iteration. We start from an initial value for the source functions, for instance $S_j^{(0)} = 0$, and perform several iterations. The mth iteration proceeds as follows:

- for each frequency ν_γ, the intensities J_j^γ are computed by solving the tridiagonal system (28) with $S_j = S_j^{(m-1)}$;
- the new source functions $S_j^{(m)}$ are computed from the J_j^γ according to Eqs. (29) and (4).

This Λ-iteration is subject to the usual problems of slow convergence when the terms ϵ_j are small and the optical depths high.

ALI. As for pure Λ-iteration, each iteration begins by the computation of J_j^γ for each frequency, solving the system (28). Then, the frequency-integrated intensity $\bar{J}_j$ is obtained by Eq. (29). Then we apply the principle of operator splitting to precondition the equations. If Λ_j^* is an approximation of the diagonal of the operator Λ_{jk}, we remove inactive photons by calculating:

$$\bar{J}_j^* = \bar{J}_j - \Lambda_j^* S_j. \tag{36}$$

Then, instead of Eq. (4), the new source functions are computed according to:

$$S_j^{(m)} = \frac{\epsilon_j B_j + \left(1-\epsilon_j\right) \bar{J}_j^*}{1 - \left(1-\epsilon_j\right) \Lambda_j^*}. \tag{37}$$

The diagonal Λ_j^* may be obtained without computing the whole operator Λ_{jk}. To this purpose, the procedure described by Rybicki & Hummer (1991, Appendix B) may be applied to the coefficients A_j, B_j and C_j of Eq. (28). In the following, this ALI method is used for all computations, except where it is explicitly stated otherwise (e.g. "semi-analytical" or "direct" method).

In addition to preconditioning, the convergence may be improved by using acceleration procedures such as those proposed by Ng (1974) or Vinsome (1976). These methods have been reviewed by Auer (1991). We plan to incorporate these methods in our scheme in the near future.

3.5. Comparison of SA and EAFD results

These two methods are based on the Eddington approximation but, in the case of EAFD, the discretization of r may introduce an extra error, which is expected to decrease when the mesh becomes finer. For the comparison, we use an homogeneous cylinder, since SA does not allow any variation of ϵ, B or κ_ν. The parameters used here are $\epsilon = 10^{-4}$, $B = 1$ and the absorption profile ϕ_ν is a Voigt profile, $\phi_\nu \propto H(a,x)$, with $a = 10^{-3}$ and x is the reduced frequency (frequency distance to the line center divided by the Doppler width). The "optical radius" $R\kappa_0$, where κ_0 is the absorption coefficient at line center, is equal to 10^5. Different cases are considered for the incident intensity: $J_\gamma^{\rm inc} = 0.03$, 0.1, 0.3, 1, 3 and 10. Values of $J_\gamma^{\rm inc}$ lower than 1 correspond to relatively hot loops, with an electron temperature higher than the brightness temperature of the solar surface (at the same wavelength). On the contrary, values greater than 1 may correspond to cool prominence threads or to far UV lines, since the brightness temperature of the Sun increases at short wavelengths. Figure 2 represents the variation of source function vs. the optical depth $\tau = \kappa_0(R-r)$. The corresponding line profiles are shown in Fig. 3. The results represented in Figs. 2 and 3 are obtained with the SA method, but the differences with those of EAFD are small, provided that the r-mesh is fine enough. This is visible in Fig. 4, where the maximum relative differences are plotted as a function of α, the number of points per decade defined in Sect. 3.3 . It appears that the error is lower than 1% for $\alpha \geq 6$ in all cases under investigation.

4. A multiray method for the two-level atom

4.1. Angular integration

By assuming fixed ratios between the different moments of intensity, the Eddington approximation reduces the problem of radiative transfer to the angle-averaged intensity J_ν, thus allowing important savings in computing time. But, as these ratios are only approximations, they introduce some error, which may be only removed by performing angular integrations of intensities I_ν. In the case of plane-parallel or spherical geometries,

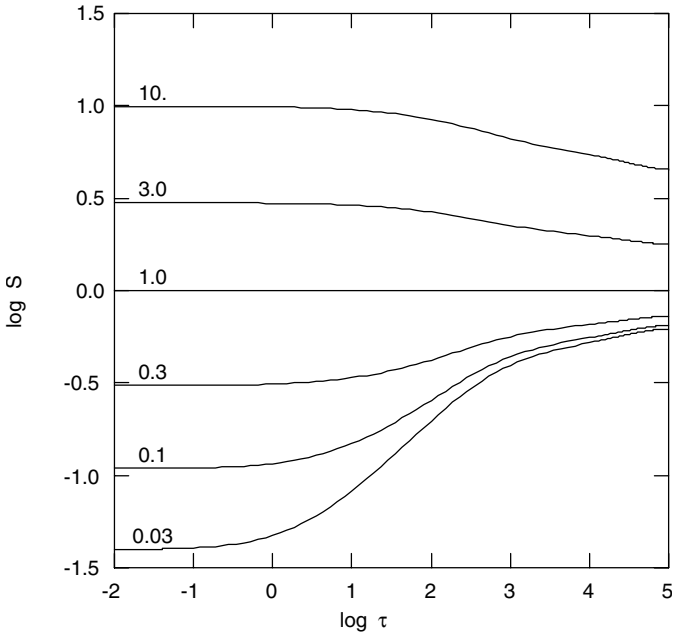

Fig. 2. Variation of source function vs. optical depth along a radius of the cylinder. Different lines correspond to different values of $J_\gamma^{\rm inc}$ from 0.03 to 10 (indicated as labels).

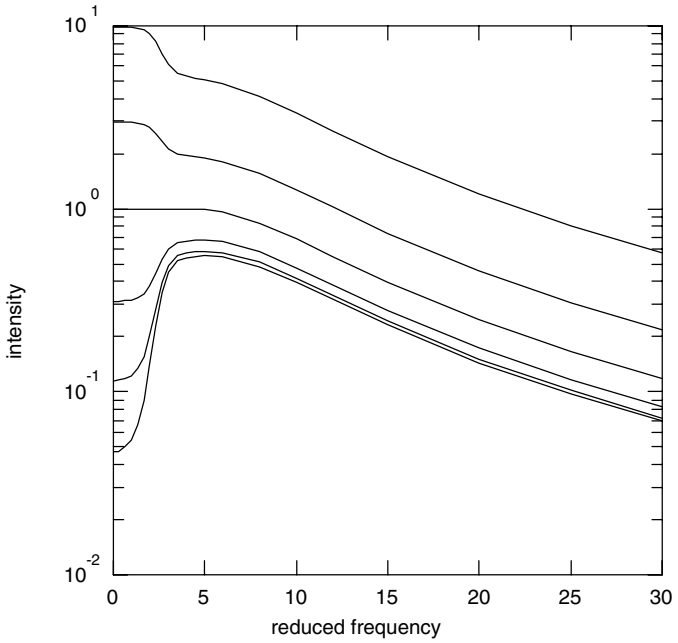

Fig. 3. Line half-profiles emitted along a ray perpendicular to the axis of the cylinder, for different values of the incident radiation $J_\gamma^{\rm inc}$, from 0.03 to 10 (intensities are increasing with the incident radiation).

it is sufficient to perform such an integration over one angle, as a result of the invariance of the problem by rotation around the vertical. In the cylindrical case, it is necessary to integrate over both angles ζ and θ. Moreover, since ζ is not constant along a ray, it is necessary to perform a separate computation of intensities for each value of r. As a consequence, the computational effort may be rather important for multiray methods, while the

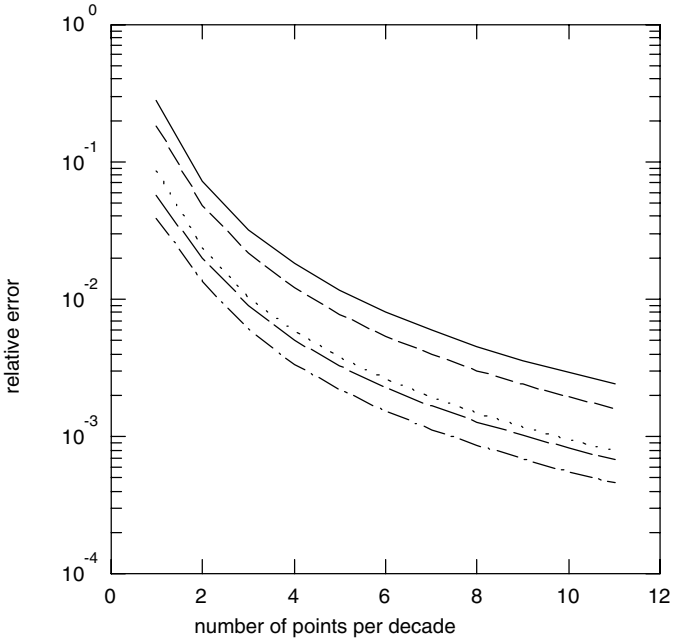

Fig. 4. Maximum relative difference between the source functions obtained with the EAFD and SA methods, as a function of the number of points per decade in the r-mesh of EAFD. Different lines correspond to different values of $J_\gamma^{\rm inc}$. Solid line: 0.03; dashed line: 0.1; dotted line: 0.3; dash-dotted line: 3; long dashes: 10. The error for $J_\gamma^{\rm inc} = 1$ is very small and does not appear on the figure.

time needed by EAFD is about the same as in the plane-parallel 1-dimension method, i.e. very short.

Thus, we introduce two new meshes for angular integration, $(\zeta_\alpha, \alpha = 1, \ldots, l)$ and $(\theta_\beta, \beta = 1, \ldots, m)$, and quadrature coefficients such that:

$$\frac{2}{\pi}\int_0^{\frac{\pi}{2}} f(\zeta)\,\mathrm{d}\zeta \approx \sum_{\alpha=1}^{l} a_\alpha f(\zeta_\alpha) \tag{38}$$

and:

$$\int_0^{\frac{\pi}{2}} f(\theta)\sin\theta\,\mathrm{d}\theta \approx \sum_{\beta=1}^{m} b_\beta f(\theta_\beta). \tag{39}$$

$(\sum_{\alpha=1}^{l} a_\alpha = \sum_{\beta=1}^{m} b_\beta = 1)$.

It is also useful to distinguish outward and inward intensities $(0 \le \zeta_\alpha \le \pi/2)$:

$$I^+_{j\alpha\beta\gamma} = I_{\nu_\gamma}\left(r_j, \zeta_\alpha, \theta_\beta\right), \tag{40}$$

$$I^-_{j\alpha\beta\gamma} = I_{\nu_\gamma}\left(r_j, \pi - \zeta_\alpha, \theta_\beta\right), \tag{41}$$

and to use the average of these two quantities:

$$Y_{j\alpha\beta\gamma} = \frac{1}{2}\left(I^+_{j\alpha\beta\gamma} + I^-_{j\alpha\beta\gamma}\right). \tag{42}$$

Finally, using the three quadrature formulae (29), (38) and (39), $\bar{J}$ is obtained from Y by:

$$\bar{J}_j = \sum_{\gamma=1}^{n} c_\gamma^j \sum_{\alpha=1}^{l} a_\alpha \sum_{\beta=1}^{m} b_\beta Y_{j\alpha\beta\gamma}. \tag{43}$$

The principle of ALI consists of evaluating the Y from the S, integrating according to (43), then applying (36) and (37) to complete the iteration.

4.2. Multiray finite-difference (MFD) method

There are different methods to compute Y from S. For instance, we also experimented with a method based on a finite-element technique, which is not presented here, since it does not provide any definite advantage with respect to the method that follows. This one is based on a finite-difference technique. Each ray is defined by three indices: j for r, α for ζ and β for θ. The shortest distance between the ray and the axis of the cylinder is:

$$r_\perp(j,\alpha) = r_j \sin\zeta_\alpha. \tag{44}$$

If ℓ is the abscissa of the running point along the ray, and $h = \ell \sin\theta_\beta$ its projection on the horizontal plane, the basic transfer equation is

$$\pm\frac{\partial I_\nu^\pm}{\partial \ell} = \kappa_\nu (S - I_\nu^\pm). \tag{45}$$

Combination of the two equations for the opposite directions, in the manner of e.g. Feautrier (1964), yields a second-degree equation for Y:

$$-\frac{\sin^2\theta_\beta}{\kappa_\nu}\frac{\partial}{\partial h}\left(\frac{1}{\kappa_\nu}\frac{\partial Y_\nu}{\partial h}\right) + Y_\nu = S. \tag{46}$$

The derivatives are transformed into finite differences with the help of a formula similar to (20), which gives another tridiagonal system for Y. As in the preceding case, the first and last equations of this tridiagonal system are provided by the boundary conditions. However, there is a difference concerning the internal boundary condition, which is located at $r = r_\perp(j,\alpha)$ instead of $r = 0$ in the case of the EAFD method. So, the number of equations in this tridiagonal system varies with j and α.

4.3. Comparison of results of EAFD and MFD

To compare the methods, we use the same models as in Sect. 3, with the number of points per decade α fixed to 7. For convenience, the numbers of grid points for ζ and θ are set equal to a common value m. The values of the source function for $m = 10$ (i.e. 100 rays for each r_j) are taken as the reference, to which we compare both the results of EAFD, and those of MFD for $m = 1, \ldots, 8$. These relative differences are represented in Fig. 5, with the value for EAFD indicated at abscissa $m = 0$, by convention. The errors corresponding to EAFD and MFD with $m = 1$ are similar (but not equal) and amount to a few percents. The errors for MFD decrease regularly with m and are lower than 10^{-2} for $m \geq 3$ and to 10^{-3} for $m \geq 7$.

4.4. Approximate diagonal operator

According to the principle of the ALI method, it is necessary to compute an approximation of the diagonal of the Λ-operator in order to accelerate the convergence, by means of formulae (36) and (37). It is possible to obtain the exact diagonal by computing the contribution of each ray with the method of

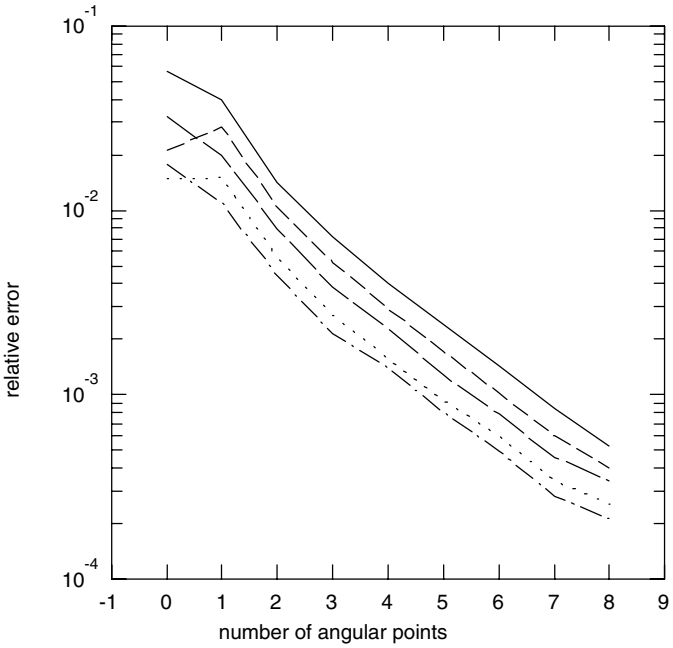

Fig. 5. Maximum relative error for the source functions obtained with the MFD method, as a function of m (common number of points for ζ and θ). Different lines correspond to different values of $J_\nu^{\rm inc}$ (same conventions as in Fig. 4). The reference is MFD with $m = 10$; $m = 0$ corresponds to EAFD.

Rybicki & Hummer (1991) and adding together the terms with appropriate coefficients (cf. Eq. (43)). In practice, it appears that the diagonal obtained by the EAFD method, which may be computed much faster, is precise enough to insure a good convergence of the process. This is illustrated in Fig. 6, where the MFD method with $m = 7$ is associated with the diagonal of the Λ-operator computed in the Eddington approximation.

5. Multilevel atoms

5.1. Statistical equilibrium equations

The statistical equilibrium equation, for the population of level i of an atom, may be written:

$$N_i \sum_{j\neq i}\left(C_{ij} + R_{ij}\right) - \sum_{j\neq i} N_j\left(C_{ji} + R_{ji}\right) = 0 \tag{47}$$

where the N_j are the level population densities, C_{ij} the collisional transition rates and R_{ij} the radiative ones. The intensity in the frequency range corresponding to a transition depends on the source function and incident intensities via the radiative transfer equation, while the source function depends on level populations. So, the Λ-iteration process for a multilevel atom with incident radiations consists of the following operations:

– to start from a given state of the radiation field, assuming for instance that internal intensities are equal to the incident intensities (optically thin approximation).

Then, alternatively:

– compute the level populations by solving the statistical equilibrium equations, which determines the source functions;

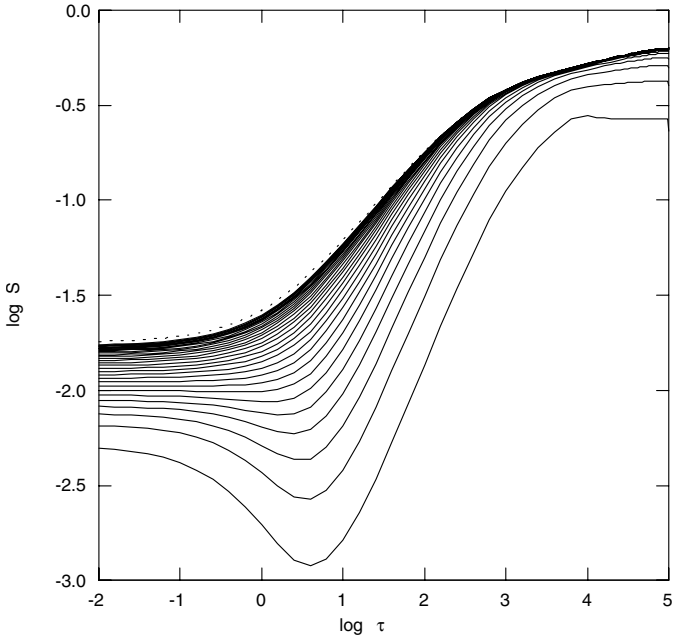

Fig. 6. Source functions vs. optical optical depth for the 30 first iterations (solid lines) of the MFD method, with use of the diagonal Λ-operator of the EAFD method. The exact solution, obtained by the direct method, is indicated by a dotted line. Parameters are: $J_\nu^{\rm inc} = 0.1$, $\alpha = 5$ and $m = 7$. Iterations start from $S = 0$.

– calculate new intensities by solving the radiative transfer equations in each line or continuum.

This process converges rapidly for optically thin transitions, but not for optically thick ones. A method to generalize preconditioning from the two-level atom to multilevel atoms has been proposed by Werner & Husfeld (1985). It was subsequently improved by different authors. In particular, Rybicki & Hummer (1991, 1992) showed how to treat overlapping lines and continua. Concerning lines, we assume complete frequency redistribution and neglect continuous absorption, so that our formulae essentially reduce to that of Werner & Husfeld (1985): we operate, in statistical equilibrium Eq. (47) the following substitutions:

$$R_{ij} = B_{ij}\bar{J}_{ij} \;\longrightarrow\; R^*_{ij} = B_{ij}\bar{J}^{\rm eff}_{ij} \tag{48}$$

and

$$R_{ji} = A_{ji} + B_{ji}\bar{J}_{ij} \;\longrightarrow\; R^*_{ji} = A_{ji}\left(1 - \Lambda^*_{ij}\right) + B_{ji}\bar{J}^{\rm eff}_{ij} \tag{49}$$

with

$$\bar{J}^{\rm eff}_{ij} = \bar{J}_{ij} - \Lambda^*_{ij}S_{ij}. \tag{50}$$

For continua, the source function depends on frequency, so that we use a slightly different sheme. The integral over frequency is replaced by a discrete sum:

$$4\pi \int_{\nu_{iq}}^{\infty} \frac{\alpha_\nu}{h\nu}\, f(\nu)\, {\rm d}\nu \approx \sum_{j=1}^{N} w_j\, f(\nu_j) \tag{51}$$

where q indicates the continuum level, ν_{iq} is the threshold frequency and α_ν the photoionization cross section. For each frequency ν_j, we compute the mean intensity J_j from the source function S_j and the incident intensities and set:

$$J^{\rm eff}_j = J_j - \Lambda^*_j S_j \tag{52}$$

where Λ^*_j is the diagonal of the monochromatic Λ-operator. So the preconditioning of a bound-free transition in statistical equilibrium Eq. (47) is operated by the following substitutions:

$$R_{iq} = \sum_{j=1}^{N} w_j J_j \;\longrightarrow\; R^*_{iq} = \sum_{j=1}^{N} w_j J^{\rm eff}_j \tag{53}$$

and:

$$R_{qi} = N_{\rm e}\Phi_{iq}(T) \sum_{j=1}^{N} w_j \left(\frac{2h\nu_j^3}{c^2} + J_j\right) {\rm e}^{-h\nu_j/kT} \;\longrightarrow$$

$$R^*_{qi} = N_{\rm e}\Phi_{iq}(T) \sum_{j=1}^{N} w_j \left[\frac{2h\nu_j^3}{c^2}\left(1 - \Lambda^*_j\right) + J^{\rm eff}_j\right] {\rm e}^{-h\nu_j/kT} \tag{54}$$

where $N_{\rm e}$ is the electron density and $\Phi_{iq}(T)$ the Saha-Boltzmann function:

$$\Phi_{iq}(T) = \frac{g_i}{2g_q}\left(\frac{h^2}{2\pi mkT}\right)^{3/2} {\rm e}^{h\nu_{iq}/kT} \tag{55}$$

(symbols have their usual meaning).

The two methods previously described for the solution of radiative transfer equations (EAFD and MFD) may be applied to deduce the intensities from the source functions, for the lines as well as for the continua.

5.2. Application to the hydrogen atom

We consider a cylinder filled with a mixture of hydrogen and helium, in the proportion of 1 atom of helium for 10 atoms of hydrogen. Helium is considered as neutral, so that only hydrogen contributes to the electron density, which is consequently equal to the proton density. The cylinder is supposed to be vertical, and defined by five parameters: temperature (T), gas pressure (P), microturbulent velocity (ξ), external radius (R) and altitude above the solar surface (H). The incident intensities are determined by solar emissions, which are the same as used by Gouttebroze & Heinzel (2002), and dilution factors which depend on H. To obtain initial populations of hydrogen levels and electron density, the equations of statistical equilibrium are solved simultaneously with those of mechanical and ionization equilibria, assuming that the intensities are constant throughout the cylinder. Then, we iterate between the level populations and the radiation field. The optical thickness of the cylinder is checked for each transition and preconditioning is applied to optically thick transitions only (usually, Lyman lines, Lyman continuum and eventually the first lines of the Balmer series). Every 10 iterations (this number is arbitrary) the electron density is updated in order to satisfy pressure equilibrium and electric neutrality.

The convergence properties of this scheme are generally good. This is illustrated in Figs. 7 and 8, which represent the variations of level populations along the axis of the cylinder

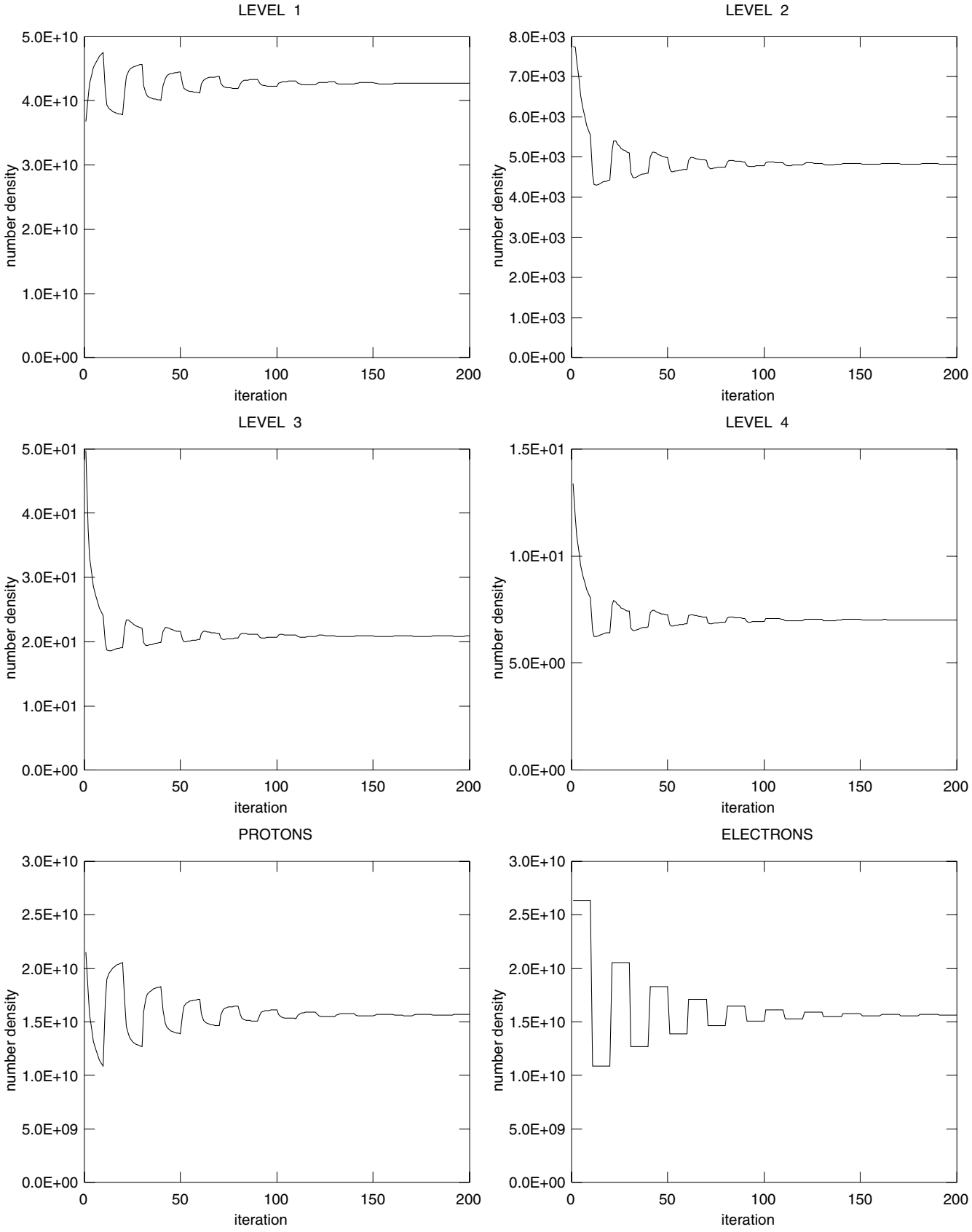

Fig. 7. Evolution of level populations, along the axis of the cylinder, during the iterative process. The hydrogen atom has 5 levels and one continuum. *Upper and median panels*: populations of the 4 lowest levels. *Lower panels*: *left*: population of the continuum level; *right*: electron density. Model parameters are: $T = 8000$ K, $P = 0.1$ dyn cm^{-2}, $R = 1000$ km, $\xi = 5$ km s^{-1}, $H = 10\,000$ km.

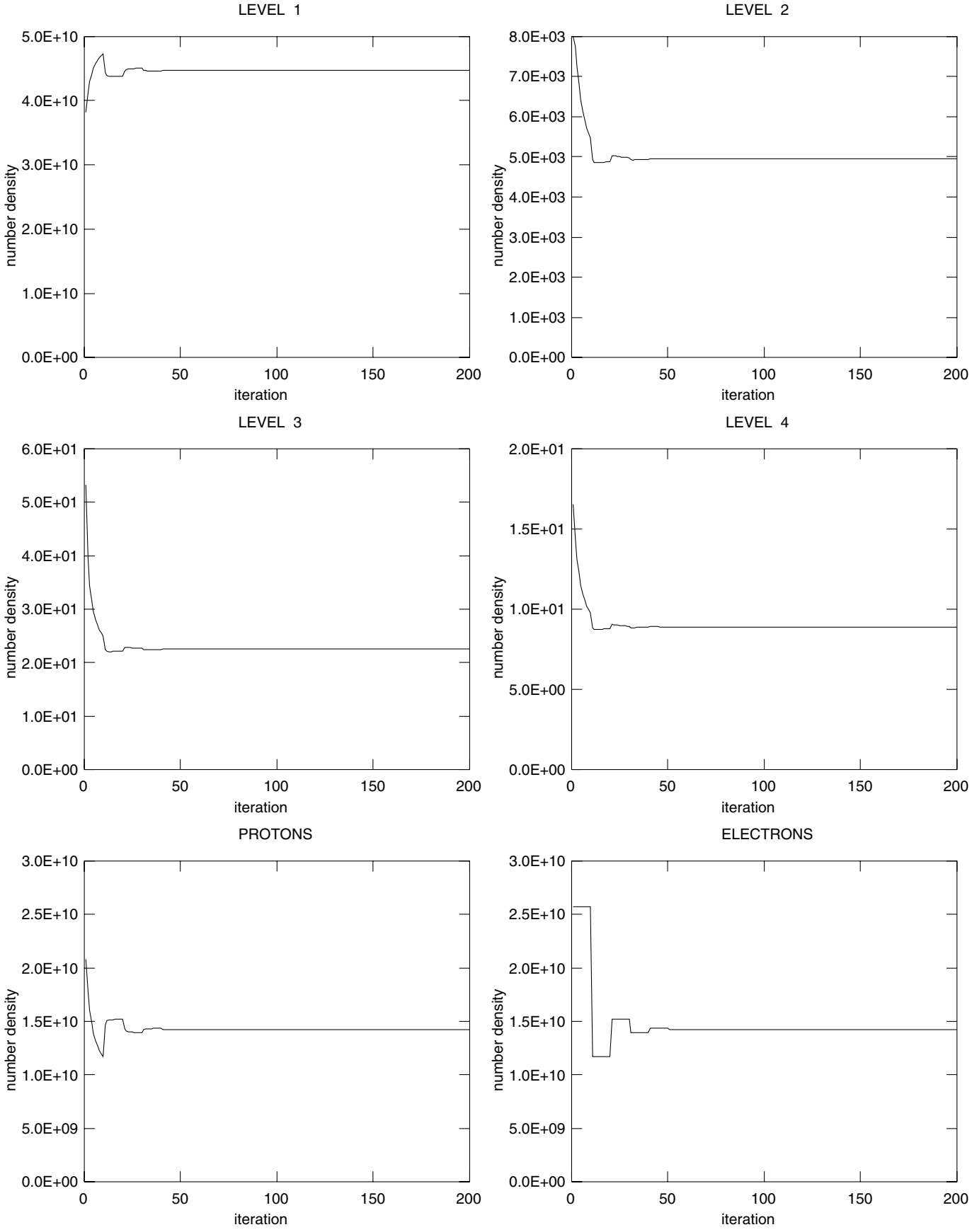

Fig. 8. Same as Fig. 7, but for a hydrogen atom with 20 levels and one continuum.

during the iteration process. Upper and median panels concern the four lowest levels of hydrogen, while lower panels show the populations of protons and electrons (these two populations are in principle equal, but they may differ during the iteration process, because the electron density is not updated at each iteration). The example shown in Figs. 7 and 8 concerns a cylinder of radius 1000 km, with a temperature of 8000 K, a pressure of 0.1 dyn cm^{-2}, a microturbulent velocity of 5 km s^{-1} and an altitude of 10 000 km. Figures 7 and 8 differ concerning the atomic model used: 5 levels+continuum for Fig. 7, 20 levels+continuum for Fig. 8. The variations are oscillatory, but those corresponding to the largest atomic models are much more damped, probably because the highest transitions, which are optically thin, have a stabilizing effect on statistical equilibrium equations. The comparison of Figs. 7 and 8 also shows that the use of a small number of levels for the hydrogen atom results in a significant reduction of the population of level 4 (and consequently of the intensity in the Hβ line) and a slight increase of electron density.

As said above, the electron density is updated every $M = 10$ iterations. This rather large number ensures a good convergence in most cases. But, in favourable cases, it may be reduced to obtain faster convergence. For instance, with the model corresponding to Fig. 7, we tried smaller values of M, from 1 to 5. The scheme appeared to be unstable for $M = 1$, but converged for $2 \leq M \leq 5$, the fastest convergence being obtained for $M = 2$. However, this property cannot be generalized: the optimum value of M seems to be model-dependent and, at least for the moment, must be determined empirically.

Finally, we compare the intensities of lines emitted by cylinders with those emitted by plane-parallel slabs, with the same physical parameters, and a thickness equal to the diameter of the cylinders. We use a set of isothermal and isobaric models, with 5 temperatures (4000, 6000, 8000, 10 000 and 15 000 K) and 9 pressures ranging from 0.002 to 1 dyn cm^{-2}, and compare the frequency-integrated intensities of several emitted lines. The diameter (or thickness for the slabs) is fixed to 2000 km, the microturbulent velocity to 5 km s^{-1} and the altitude to 10 000 km. For slabs, the intensity (E_p) is measured perpendicularly to the surface while, for cylinders, we consider the intensity (E_c) emitted along a ray perpendicular to the axis. For the 4 first lines of the Lyman series and the 3 first Balmer lines, the ratio (E_c/E_p) remains in the range [0.61, 1.21]. The variation of this ratio as a function of pressure seems rather complicated for Balmer lines, as well as for Lα.

For higher Lyman lines, the variation is more regular and may be illustrated by Fig. 9 (which corresponds to Lγ): the ratio is almost independent of pressure and remains close to 1 for low temperatures (4000 and 6000 K). For higher temperatures, the ratio is generally decreasing with pressure. In fact, at low temperatures, the variations of intensity with pressure are small: thermal emission is negligible and the emitted intensity principally comes from the reflexion of incident radiation. At higher temperatures, the photons produced by collisions inside the object become more and more important as the temperature increases. It seems that the intensity grows more rapidly in the slabs than in the cylinders because the slabs ensure a better confinement of radiation.

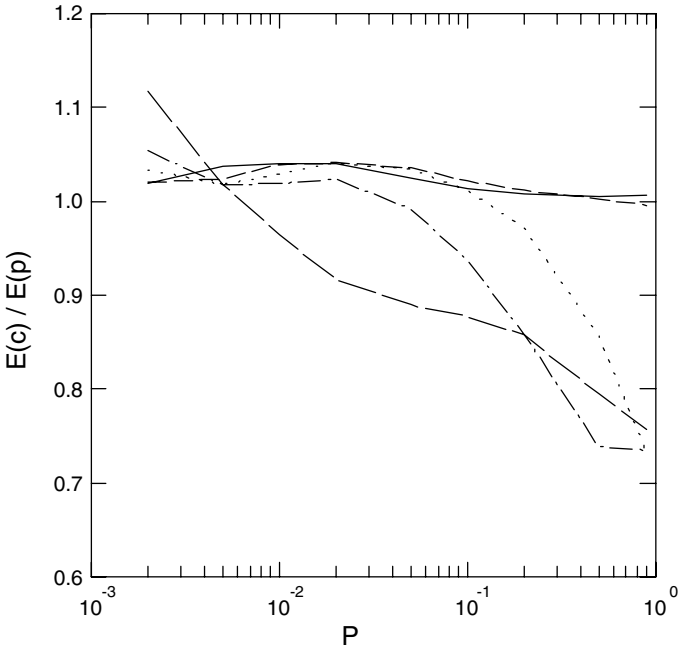

Fig. 9. Ratio of frequency-integrated emitted intensities E_c/E_p for the Lyman-γ line of hydrogen (E_c: cylinders, E_p: plane-parallel slabs). Abscissae: pressure in dyn cm^{-2}. Each curve corresponds to a different temperature: solid line: 4000 K, short-dashed line: 6000 K, dotted line: 8000 K, dash-dotted line: 10 000 K, long-dashed line: 15 000 K.

6. Conclusion

A numerical method to solve NLTE radiative transfer problems in cylindrical geometry has been developed. It is restricted to one-dimension problems, but allows the treatment of multilevel atoms of arbitrary complexity. Two different versions are proposed under the same principle of accelerated Λ-iteration (ALI): one assuming the Eddington approximation (EAFD), the other (MFD) treating in detail the transfer along a large number of rays. The first one is as fast as the corresponding ALI method for plane-parallel slabs. The second one is slower than EAFD, but is as precise as the variable Eddington factor methods of Leung (1976) or Heasley (1977). It is possible to obtain a fast and precise method by first using EAFD until convergence, and performing a few MFD iterations to refine the results.

Some further developments are under study. In particular, we plan to introduce partial frequency redistribution in resonance lines, to improve the treatment of hydrogen Lyman lines. The extension to multidimensional cylindrical problems is also envisaged. In future papers, we plan to apply the present method to the construction of multithread prominence models, and extend it to other atomic species, especially helium, magnesium and calcium.

Acknowledgements. I wish to thank H. Frisch for critical reading of the manuscript. I acknowledge fruitful discussions with F. Paletou and J.-C. Vial. Many constructive comments from the referee contributed to improve this paper.

References

Auer, L. H. 1991, in Stellar Atmospheres: Beyond Classical Models, ed. L. Crivellari, I. Hubeny, & D. G. Hummer, NATO ASI Series C341 (Dordrecht: Kluwer), 9

Chandrasekhar, S. 1950, Radiative Transfer (London: Oxford University Press)

Feautrier, P. 1964, C. R. Acad. Sci. Paris, 258, 3189

Gouttebroze, P. 1990, A&A, 228, 295 (G90)

Gouttebroze, P., & Heinzel, P. 2002, A&A, 385, 273

Gouttebroze, P., Vial, J.-C., & Tsiropoula, G. 1986, A&A, 154, 154

Heaslet, M. A., & Warming, R. F. 1966, JQSRT, 6, 751

Heasley, J. N. 1977, JQSRT, 18, 541

Hubeny, I. 2003, in Stellar Atmosphere Modeling, ed. I. Hubeny, D. Mihalas, & K. Werner, ASP Conf. Ser., 288, 17

Leung, C. M. 1976, JQSRT, 16, 559

Ng, K. C. 1974, J. Chem. Phys., 61, 2680

Paletou, F. 2001, C. R. Acad. Sci. Paris, 2, Série IV, 885

Rybicki, G. B. 1971, JQSRT, 11, 589

Rybicki, G. B., & Hummer, D. G. 1991, A&A, 245, 171

Rybicki, G. B., & Hummer, D. G. 1992, A&A, 262, 209

van Noort, M., Hubeny, I., & Lanz, T. 2002, ApJ, 568, 1066

Vinsome, P. K. W. 1976, in Proceedings of the Fourth Symposium on Reservoir Simulation, Society of Petroleum Engineers, 149

Werner, K., & Husfeld, D. 1985, A&A, 148, 417

Wick, G. C. 1943, Z. Phys., 121, 702